DENSITY-SENSITIVITY STUDY ABOUT NONLINEAR MULTIPARAMETER PRESTACK INVERSION BASED ON THE EXACT ZOEPPRITZ EQUATION

QIANG GUO[1], HONGBING ZHANG[1], LIFENG LIANG[2], ZUOPING SHANG[3] and GUOJIAO HUANG[1]

[1] College of Earth Science and Engineering, Hohai University, Nanjing 210098, P.R. China. hbzhang@hhu.edu.cn
[2] Department of Geography, Lingnan Normal University, Zhanjiang 524048, P.R. China.
[3] College of Mechanics and Materials, Hohai University, Nanjing 210098, P.R. China.

ABSTRACT

Guo, Q., Zhang, H.B., Liang, L., Shang, Z.P. and Huang, G.J., 2018. Density-sensitivity study about nonlinear multiparameter prestack inversion based on the exact Zoeppritz equation. *Journal of Seismic Exploration*, 27: 277-300.

　　　　Density information is of critical in identifying the presence and estimating the saturation of hydrocarbon in the reservoir. However, density is difficult to estimate based on conventional prestack inversion approach. In addition, prestack inversion is a nonlinear and ill-posed problem. In order to alleviate the ill-posedness and obtain reliable density information, we propose a nonlinear multiparameter prestack inversion method by constructing the edge-preserving regularized objective function based on anisotropic Markov random fields; we make an attempt to directly use the exact Zoeppritz equation and employ fast simulated annealing algorithm to solve the nonlinear optimization problem. Numerical analysis indicates that density parameter contributes relatively greater on altering the reflectivity magnitude at small incidence angle. In 2D synthetic test, we employ different gathers with specified angle range to test the inverted results and analyze the sensitivity of density. The synthetic results demonstrate that we can obtain reliable density result with small incidence angle by the proposed inversion method. In addition, density results can be improved by scaling the regularization term of density. The inverted density from the field data reveals detailed structural information and shows good agreement with the logging curves; the satisfactory density inverted results from small angle gather validates the conclusion from the numerical results.

KEY WORDS: density-sensitivity, prestack seismic inversion, exact Zoeppritz equation,
　　　　　　　edge-preserving regularization, Markov random field.

INTRODUCTION

Prestack seismic inversion methods based on amplitude variation with offset (AVO) theory (Ostrander, 1984; Downton and Ursenbach, 2006; Chapman et al., 2006) has already established itself as one of the most powerful methods for estimating subsurface petrophysical properties. Compared to conventional post-stack inversion, prestack inversion can overcome the limited information of stacked seismic data from vertical incidence and it can simultaneously obtain multiple elastic parameters, such as P-wave velocity (V_P), S-wave velocity (V_S), and density (ρ). In particular, density has long been recognized as a potential seismic indicator of fluid saturation because of its linear relationship with porosity. In addition, given its dependence on mineral composition, density can also be a diagnostic for lithology. Therefore, a robust methods of density estimation based on prestack seismic inversion is of great importance for oil and gas exploration.

The intrinsic nonlinearity of the Zoeppritz equation makes it less pragmatic in practical application. Consequently, its linearized approximations (e.g., Bortfeld, 1961; Aki and Richards, 1980; Shuey, 1985; Fatti et al., 1994) have been derived and utilized instead. However, these linearized approximations are restricted to weak-contrast boundaries and not-too-large-offset cases (Aki and Richards, 1980), reducing the accuracy of inverted results. In particular, Grossman (2003) pointed out that the linearized approximations of the Zoeppritz equation for P-wave reflectivity are relatively insensitive to changes in density, especially for limited-aperture experiments (Lines, 1998; Ursenbach, 2002). Therefore, using the exact Zoeppritz equations would be able to obtain density information with more accuracy (Downton, 2005; Zhi et al., 2016). In addition, the complex operator relating the model and data of prestack inversion remains a highly nonlinear problem. In order to alleviate the nonlinearity and obtain a unique solution, regularization strategy has often been used (Tarantola, 2005; Sacchi et al., 2006). In particular, edge-preserving regularization (EPR) (Youzwishen and Sacchi, 2006; Misra and Sacchi, 2008; Zhang et al., 2009; Theune et al., 2010; Guo et al., 2016), by which the inverted results are regularized while the geological edges or structures (e.g., faults, channel, and fractures etc.) are preserved, has proved to be an effective technique. Moreover, model nonuniqueness also cause local minima in the inversion. In such cases, linearized or gradient-based optimization approaches (Tarantola and Vallete, 1982; Tarantola, 2005) usually highly depend on the initial model and fail to reach the global minimum. In absence of sufficient prior information, global-optimization techniques could obtain better results, such as simulated annealing algorithm (Sen and Stoffa, 1996; Ma, 2002; Chen et al., 2006), particle swarm optimization (Yan and Gu, 2013; Paasche and Tronicke, 2014), and genetic algorithm (Ji et al., 2000; Aleardi and Mazzotti, 2017). In particular, the fast simulated annealing (FSA) algorithm (Varela et al., 2006; Zhang et al., 2009; Sen and Stoffa, 2013) has been widely applied in geophysical inversion problem because it can obtain a global optimum result without depending on the initial model.

Difference between inverted parameters can significantly destabilize the results of multiparameter inversion. This comes down to the sensitivity of elastic parameters to seismic amplitude variations. Zong et al. (2012, 2013) proposed that the density term embedded in the fluid or Young's modulus is difficult to estimate because it is less sensitive to seismic amplitude variations, and the indirect way can create more uncertainty for the estimation of Young's modulus and Poisson's ratio. Ji et al. (2000) developed the sensitivity study of elastic parameters, in which amplitude variation with slowness for small- and large-offset seismic data is presented, in order to handle the non-linearity beyond the critical slowness. For the sensitivity of density, it is commonly believed that, compared with velocity parameters, density is relatively difficult to be accurately estimated because of its insensitivity to amplitude variations based on the linearized approximations (Downton, 2005; Zhi et al., 2016). In order to obtain reliable density information, scholars have made great efforts. Liang et al. (2017) proposed the improved Fatti's equation in which the sensitivity of the coefficient associated with density to angle variation is enhanced. Huang et al. (2011) analyzed the consistency of multiparameter in prestack inversion and proposed a constrained inversion approaches which improves the accuracy of the three parameters. In a word, it is worthwhile to conduct further analysis on the sensitivity of density and the associated prestack inversion method to obtain density information, especially based on the exact Zoeppritz equation.

In this paper, we propose a nonlinear prestack inversion method by constructing the objective function including edge-preserving regularization based on anisotropic Markov random fields; we employed FSA algorithm to solve the nonlinear optimization problem and we make an attempt to directly use the exact Zoeppritz equation. In particular, we focus our attention on the sensitivity of density by investigating its contribution on altering the reflectivity magnitude at different incidence angles. We test the inverted results by using different gathers with specific angle range; we improve density results by adjusting the weighting coefficient of the corresponding regularization term. Aided by the proposed inversion method, we can obtain satisfactory density results by using small angle range.

This paper mainly consists of three parts. First, we build the objective function with edge-preserving regularization. Then, we analyze the density-sensitivity by investigating the angle-dependent contribution on altering the reflectivity magnitude. Finally, we demonstrate our method and conclusion by both synthetic data test and field data example.

METHODOLOGIES

Forward operator

The Zoeppritz equation mathematically depicts the exact reflection and transmission coefficients as a function of incidence angle and six seismic parameters (i.e., P- and S-wave velocities, and density of the upper and lower

medium) when plane wave strikes an elastic boundary. The matrix form of the exact Zoeppritz expression can be written as (Aki and Richards, 1980)

$$
M \begin{bmatrix} R_{PP} \\ R_{PS} \\ T_{PP} \\ T_{PS} \end{bmatrix} = \begin{bmatrix} -\sin\theta_1 \\ \sin\theta_1 \\ -\cos2\varphi_1 \\ \sin2\varphi_1 \end{bmatrix} ,
\tag{1}
$$

$$
M = \begin{bmatrix} \sin\theta_1 & \cos\varphi_1 & -\sin\theta_2 & -\cos\varphi_2 \\ \cos\theta_1 & -\sin\varphi_1 & \cos\theta_2 & -\sin\varphi_2 \\ \cos2\varphi_1 & -\dfrac{v_{S1}}{v_{P1}}\sin2\varphi_1 & -\dfrac{\rho_2}{\rho_1}\dfrac{v_{P2}}{v_{P1}}\cos2\varphi_2 & \dfrac{\rho_2}{\rho_1}\dfrac{v_{S2}}{v_{P1}}\sin2\varphi_2 \\ \sin2\theta_1 & \dfrac{v_{P1}}{v_{S1}}\cos2\varphi_1 & \dfrac{\rho_2}{\rho_1}\dfrac{v_{S2}^2 v_{P1}}{v_{S1}^2 v_{P2}}\sin2\theta_2 & \dfrac{\rho_2}{\rho_1}\dfrac{v_{S2}v_{P1}}{v_{S1}^2}\cos2\varphi_2 \end{bmatrix} ,
\tag{2}
$$

where M is the coefficient matrix; R is the reflection coefficient; T is the transmission coefficient; v is the velocity; ρ is the density; subscripts P and S denote P-wave and S-waves, respectively; subscripts 1 and 2 denote the upper and lower media across the interface, respectively; θ_1 and θ_2 are P-wave incidence and transmission angles, respectively; φ_1 and φ_2 are S-wave reflective and transmission angles, respectively. We directly used eq. (1) as the forward operator to calculate R_{PP} in the inversion. By introducing the exact Zoeppritz equation, instead of inverting the velocity and density contrasts (or reflectivities) as done in most linearized prestack inversions (Kabir et al., 2006; Ma, 2002), we directly inverted the three parameter values (P- and S-wave velocities and density) in order to reduce the accumulation error and analyze the sensitivity of density parameters.

Objective function

We based our prestack seismic inversion on the convolutional model between the reflectivities and source wavelet. Assuming that earth structure is represented by a series of lateral layers with constant material properties separated by planar interfaces, the earth model can be represented by a discretized model parameter vector m. Therefore, for an one-dimension Earth model, a seismogram d in discrete form can be expressed as

$$
d(\theta) = w(\theta) * r(m, \theta) + e ,
\tag{3}
$$

where $d(\theta)$ is the observed data (angle gather) corresponding to incidence angle θ; m is the discretized unknown model parameters, i.e., $m=[V_{P1}\ V_{P2} \dots V_{PN};\ V_{S1}\ V_{S2} \dots V_{SN};\ \rho_1\ \rho_2 \dots \rho_N;]$; $r(\theta, Z)$ is PP reflection coefficient of incidence angle which can be calculated by eq. (1); $w(\theta)$ is the source wavelet

of incidence angle; e is the random noise that is assumed to follow a zero-mean Gaussian distribution with variance σ^2, and * denotes the convolution operator.

Seismic inversion problem is defined as an optimization procedure aiming at finding the model parameters that best fits with the observed data, which is expressed as a measurement of the misfit between the observed and the modelled data

$$F_1(m) = \frac{1}{2\sigma^2} \|d(\theta) - w(\theta) * r(m, \theta)\|^2 . \tag{4}$$

However, seismic inversion is usually an ill-posed problem which is highly nonlinear and unstable. To alleviate the nonlinearity and make the problem well-posed, we incorporated prior constraints to regularize the inversion problem. By introducing the prior information or constraints to a maximum a posterior (MAP) framework (Charbonnier et al., 1997), the regularized objective function F can be rewritten as

$$F(m) = F_1(m) + \lambda_1 \cdot F_2(m) + \lambda_2 \cdot F_3(m)$$

$$= \frac{1}{2\sigma^2} \|d(\theta) - w(\theta) * r(m, \theta)\|^2 + \lambda_1 \cdot \sum_{C_{1k}} \phi\left(D_C^k(m)/\delta\right) + \lambda_2 \cdot \sum_{C_{2k}} \phi\left(D_C^k(m)/\delta\right), \tag{5}$$

where F_1 is the fidelity term; F_2 is the prior (regularization) term; F_3 is the constraint term from the logging data; m includes the inverted parameters (i.e., V_P, V_S, and density); $D^k{}_C(\cdot)$ is the gradient function calculating the model gradient; and ϕ is a potential (regularization) function. Note that F_2 and F_3 introduce the penalty of the model parameter and the logging data, respectively. In Eq. (5), three regularization parameters are employed, i.e., trade-off parameters λ_1 and λ_2 which control the weight of the three terms, and scaling parameter δ which tunes the model gradient $D(m)$ value above which a discontinuity is detected. According to Markov random field (MRF) approach (Charbonnier et al., 1997), k ($k = 1$, 2, and 3) denotes the MRF order which controls the smoothness of the model parameter; C_{1k} and C_{2k} denote data cliques in MRF neighbourhoods which correspond to first-order, second-order, and kth-order neighbourhoods. We will focus on discussing data cliques (C_{1k} and C_{2k}) and MRF order (k) in the next section. For multiparameter inversion, the prior term F_2 takes the form of

$$F_2 = \lambda_D \cdot F_{2D}(\rho) + F_{2P}(V_P) + F_{2S}(V_S) \quad , \tag{6}$$

where F_{2P}, F_{2S}, and F_{2D} are the prior (regularization) terms of V_P, V_S, and ρ, respectively. Note we add a weighting coefficient λ_D to scale the prior term of density (we will demonstrate that density result can be improved by properly adjusting λ_D in the synthetic test). Then F_2 can be rewritten as

$$F_2 = \lambda_D \cdot \sum_{C_{1k}} \phi\left(D_C^k(\rho)/\delta_D\right) + \sum_{C_{1k}} \phi\left(D_C^k(V_P)/\delta_P\right) + \sum_{C_{1k}} \phi\left(D_C^k(V_S)/\delta_S\right) \quad , \quad (7)$$

where the scaling parameters δ corresponding to the three parameters (δ_P, δ_S, and δ_D) are different, respectively. Note that the constraint term F_3 is only used along the traces where logging data are available.

In particular, the prior information or constraints imposed on the objective function in eq. (5) is expressed through the form of potential function, which assigns a penalty to every value of the model gradient (discontinuity). Table 1 lists several commonly used potential functions and Fig. 1 shows their prior probability distributions to illustrate the edge-preserving properties. In Fig. 1, non-quadratic function ϕ_{GM} has the highest and widest two wings of the prior probability distribution, which indicates that the probability of accepting a large gradient for ϕ_{GM} is maximal. Therefore, ϕ_{GM} can preserve edges or boundaries well. On the other hand, quadratic function ϕ_{Gauss} has the narrowest wings of distribution and thus indicating the minimal probability of accepting gradients, therefore it usually causes inverted results over-smoothed.
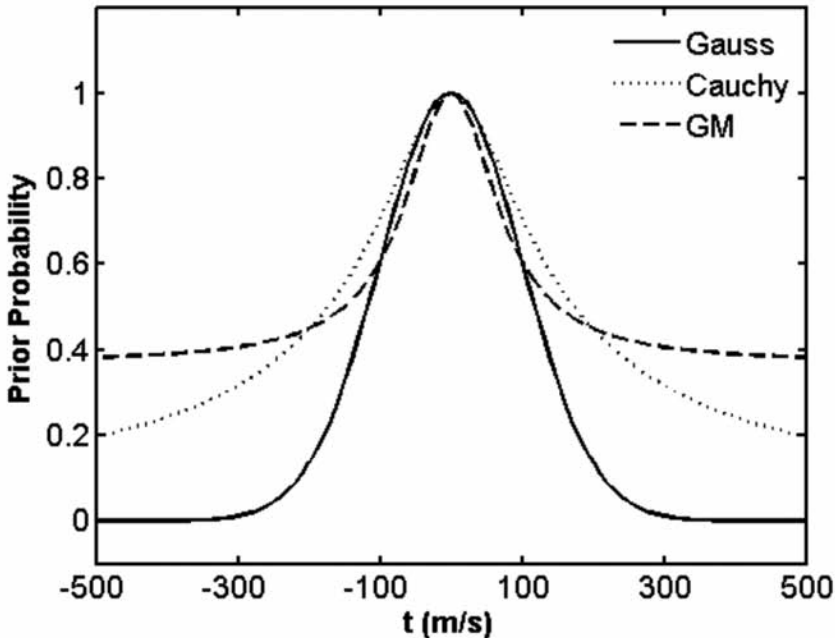

Fig. 1. The prior probability distributions of the potential functions listed in Table 1. They represent the gradient of velocity for example.

Table 1. Potential functions (ϕ_{GM}, ϕ_{Gauss}, and ϕ_{Cauchy}) and their associated weighting functions.

Potential function	Expression
ϕ_{Gauss}	t^2
ϕ_{GM}	$\dfrac{t^2}{1+t^2}$
ϕ_{Cauchy}	$\log(1+t^2)$

Anisotropic Markov Random Field neighborhoods

Now we discuss the MRF order k and the data cliques C (C_1 or C_2) in MRF neighborhoods in eq. (5). The prior term F_2 is the k-th order smoothness on the prior information (Geman and Reynolds, 1992). For the central point S shown in Fig. 2, the points numbered with 1, 2, and 3 are the first- ($k = 1$), the second- ($k = 2$), and the third- ($k = 3$) order MRF neighborhoods, respectively, and they correspond to piecewise constant, planar, and quadratic models, respectively. For $k = 1$, 2, and 3, C_{1k} represent three types of the first-order cliques (including diagonal adjacent points, involving two points), three types of the second-order cliques (involving three or four points), and four types of the third-order cliques (involving four or six points), respectively. The details of calculating the gradient functions $D^k{}_C(m)$ for the cliques C_{1k} ($k = 1,2,3$) can be referred to Geman and Yang (1995) and Zhang et al. (2007). Note that C_{1k} includes horizontal, vertical, and diagonal directions, and C_{2k} for the constraint term of logging data only contains vertical direction along the wells available. Obviously, the order of the neighborhoods determines the ranges affected by the constraint data. By analyzing the results of field logging data, Zhang et al., (2007) pointed out that low-order neighborhood keeps most feature (high-frequency components) of logging curve, while high-order neighborhood roughly depicts the edges with large gradients (only leaving low-frequency trend). Therefore, we take consideration of this characteristic and we adopt multiple MRF orders strategy in the inversion, i.e., making use of high order neighborhoods to wide-range search at early stage and low order neighborhoods to locally search at late iterations.

However, the MRF neighborhoods introduced above are aimed at isotropic media. In our case, we propose to properly select the cliques of the neighborhoods in anisotropic media. Considering transversal continuity in layered formation, we use all cliques of the first-order neighborhoods and all horizontal cliques of the second- or third- order neighborhoods; however, we cautiously use vertical cliques of the second- or third-order neighborhoods because those may lead to instabilities. Then we propose the anisotropic Markov random field (AMRF) neighborhoods, and the prior term F_2 can be rewritten as

$$F_2(m) = \sum_{C_{1k}} \alpha_C^k \cdot \phi\left(D_C^k(m)/\delta\right) \quad , \tag{8}$$

where α^k_C are the weighting coefficients which adjusts the model gradient value $D(m)$ in different directions for AMRF neighborhoods. In eq. (8), the coefficients α^k_C influence the role of gradient functions directionally. For the transverse isotropic layered formation, we need to adjust α^k_C values in the four directions in order to balance horizontal and vertical gradient functions. Large value of α^k_C in horizontal direction can only allow small gradients to be accepted, thus preserving lateral continuity of the layered formation; in contrast, small value of α^k_C in vertical direction permits large gradients across interface to be accepted, which is helpful to large longitudinal gradient of interlayers.

Fig. 2. The neighborhood system of Markov random field for the point S. The first-order neighborhood consists of four points labeled by 1. The *n*th order neighborhood consists of the points labeled by the numbers smaller than or equal to *n*. Note horizontal adjacent points are adjacent traces and vertical adjacent points are adjacent samples.

Optimization approach

The inversion procedure is an optimization approach which minimizes the objective function F in eq. (5). Considering the highly nonlinear relationship between the observed data and the model parameters, we employ FSA algorithm to achieve the global optimum. Compared to linearized inversion methods, FSA can achieve globally optimal solution without depending on initial model or being trapped into local minimal. We follow the FSA procedure proposed by (Ingber, 1989). The perturbation of the next candidate point of inverted parameters is expressed as

$$m^{(k+1)} = m^{(k)} + T^{(k)} \cdot sign(\gamma - 0.5) \cdot [(1 + 1/T^{(k)})^{|2\gamma - 1|} - 1] \cdot (m_{max} - m_{min}), \quad (9)$$

where $m^{(k)}$ and $m^{(k+1)}$ are the current and perturbed value, respectively; $[m_{min}, m_{max}]$ are the range to which the model values are limited; γ represents random numbers of $[0, 1]$; $sign(\cdot)$ is the sign function; $T^{(k)}$ is the current temperature, starting with the initial temperature $T^{(0)}$, which follows the cooling schedule as

$$T^{(k)} = T^{(0)} \exp\left(-ck^{1/n}\right) \quad ,$$ (10)

where c is the damping coefficient; and n is the dimension of the inverted parameters. The initial temperature $T^{(0)}$ is determined by the empirical equation

$$\exp\left(-\frac{\overline{\Delta E}}{T^{(0)}}\right) = X \ ,$$ (11)

where $\overline{\Delta E}$ is the average increment of the energy; X is the initial acceptance probability, which is closed to but not equal to 1, (e.g., $X = 0.9$). In each iteration, the perturbed value is conditionally accepted according to the acceptance probability P, which is expressed as

$$P = \left[1 - (1 - h) \cdot \frac{\Delta E}{T^{(k)}}\right]^{1/(1-k)} \quad ,$$ (12)

where ΔE is the energy difference between the current and perturbed model of the objective function in the k-th iteration, and h is a constant.

According to the acceptance criterion, the perturbed value is unconditionally accepted if the cost function is small (negative variation) relative to the previous point. If the perturbed value results in a higher cost function (positive variation), then the perturbed value may still be accepted. In the next section, we will discuss the angle-dependent contribution of density on altering the reflectivity magnitude and the corresponding influence on the acceptance probability at different incidence angles.

DENSITY-SENSITIVITY ANALYSIS

In this part, inspired by the work conducted by Kabir et al. (2006), we numerically analyzed the sensitivity of density based on its contribution on altering the reflectivity magnitude at different incidence angles (angle-dependent reflectivity contribution). However, in our work, we directly analyzed the three elastic parameters by using the exact Zoeppritz equation, instead of their reflectivities; we also extended the analysis to three AVO

classification models to gain confidence in the conclusion. Three models of typical (Hilterman, 2001) (listed in Table 2) are employed for the analysis.

Table 2. Model parameters for three AVO classification (Hilterman, 2001).

		V_p (m/s)	V_s (m/s)	Density (g/cm^3)
Model 1 (Class III AVO)	Overlying Shale	2191	818	2.16
	Gas Sand	1542	901	1.88
Model 2 (Class II AVO)	Overlying Shale	2642	1166	2.29
	Gas Sand	2781	1665	2.08
Model 3 (Class I AVO)	Overlying Shale	3093	1515	2.40
	Gas Sand	4050	2526	2.21

Fig. 3(a)–(i) shows the distribution curves for analyzing the sensitivity (reflectivity contribution) for the three elastic parameters. In each sensitivity analysis, we vary the value of the parameter of interest and set the values of other two parameters fixed. We can find that density (Figs. 3(a), 3(d), and 3(g)) contributes greater on altering the reflectivity magnitude at small incidence angle, because the divergence of the (five) distribution curves (generated by varying the density value) is most significant at small incidence angle and these curves gradually converge when increasing the incidence angle. This trend can be observed in all the three models. In contrast, velocities generally demonstrate the opposite trend, i.e., they contribute less on altering the reflectivity magnitude at small incidence angle and the contribution increases at large incidence angle. This is particularly true for V_s (Figs. 3(c), 3(f), and 3(i)) in the three models and V_p [Figs. 3(e) and 3(h)] (except for Model 1, in which the corresponding contribution is similar at different angles). Therefore, based on the analysis of angle-dependent reflectivity contribution, density parameter is sensitive at small incidence angle and velocity parameters are sensitive at moderate or large incidence angle.

Furthermore, the property of density's angle-dependent reflectivity contribution will effect the inversion results based on the proposed inversion method. During the nonlinear inversion procedure, the perturbed density is randomly generated according to eq. (9), because of the larger reflectivity contribution at small incidence angle for density, the perturbed density will consequently generate large energy difference ΔE in eq. (12) and increase the probability to be accepted (or rejected). Therefore, we can obtain fine and stable result of density by inverting the angle gather with small incidence angle. Next, we need to verify the numerical results by testing synthetic and field data.

Class III
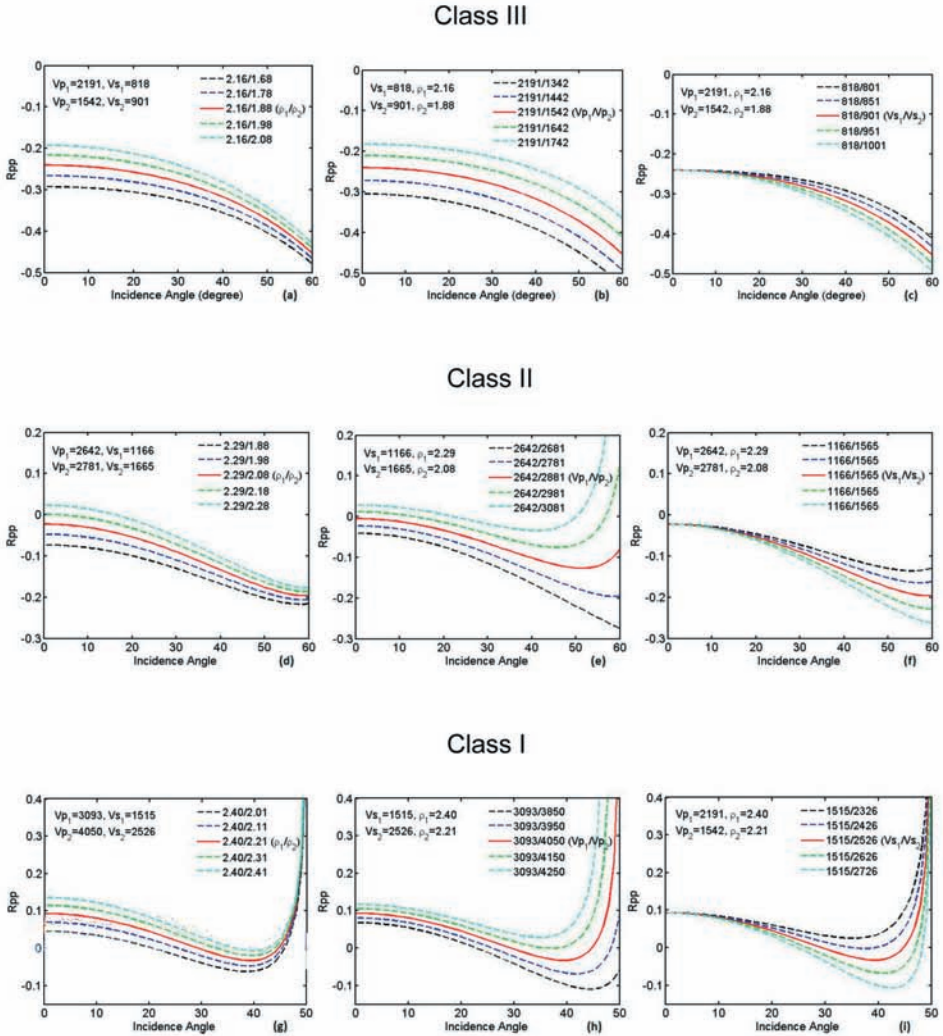

Class II

Class I

Fig. 3. The distribution curves for analyzing the sensitivity (reflectivity contribution) of density (a, d, and g), V_P (b, e, and h), and V_S (c, f, and i). The red solid lines represent the distribution curves for the three models listed in Table 2, respectively. The dash lines are generated by varying the corresponding analyzed parameter. The units of velocities and density are m/s and g/cm^3, respectively.

SYNTHETIC DATA TEST

In this section, we demonstrated the proposed inversion method by inverting the three parameters (V_P, V_S, and density) for synthetic data. In particular, we tested the inverted density results by using different incidence angles and by adjusting the weighting coefficient of the density prior term.

The synthetic data for a 2D faulted anticline is prepared for the test (its true models are shown in Figs. 4(a)–(c)). There are 61 CDPs and 175 samples (2 ms sampling rate). Every CDP (angle gather) has 17 angle traces ranging from 0° to 48° with an angle interval of 3°. Three angle wavelets, corresponding to the near-, middle-, and large-offset, are zero-phase Ricker wavelets with dominant frequencies of 35, 33, and 31 Hz, respectively. Fig. 4(d) shows the initial model of V_P. The initial model of V_S and density are built as a function of V_P. In order to introduce the constraint term F_3 in the synthetic test, we took the 15th and 45th traces of the model as pseudo-wells and extract their parameters as logging data.
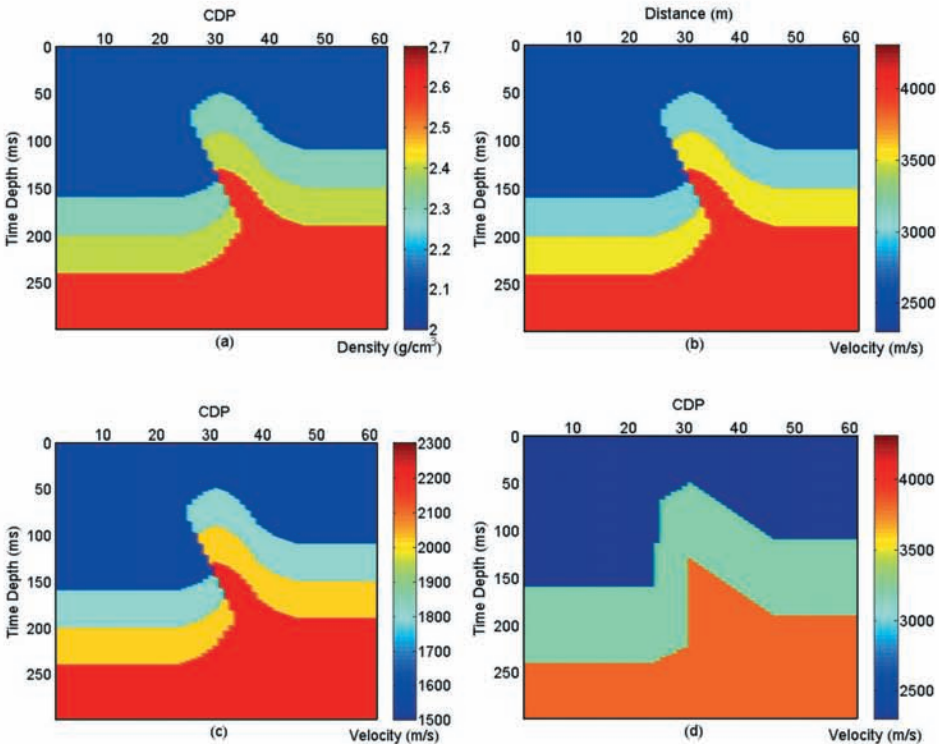
Fig. 4. The true models of (a) density, (b) V_P, (c) V_S, and (d) the initial V_P model starting for the inversion.

In the test, the initial values of λ_1 and λ_2 were set to be 0.3 and 0.6, respectively, and the initial values of δ corresponding to V_P, V_S, and density were set to be 250, 200, and 0.18, respectively. The optimization approach was the FSA with an initial temperature $T^{(0)} = 0.05$ and a temperature damping coefficient $c = 0.9$ (annealing until reaching the threshold temperature of 0.00001). We adaptively adjusted the regularization parameters (λ and δ) in the inversion, i.e., gradually decreasing λ values and increasing δ values during the annealing process. The regularization

parameters were estimated by the maximum likelihood method which was given by Zhang et al. (2007) in detail. Here only the first-order MRF neighborhoods are tested.

Testing the results of density with different angle gathers

The angle gathers (corresponding to small, moderate, and large incidence angle) prepared for the test are 1) from 0° to 12°, 2) from 21° to 33°, and 3) from 36° to 48°. Figs. 5(a)–(i) shows the inverted results of density, V_P, and V_S by using the (three) angle gathers, respectively, and Figs. 6(a)–(i) show the residuals of the inverted results with the corresponding true models, respectively.

For the inverted results of density (Figs. 5(a)–(c)), we find the result by using the small incidence angle is better after comparing the three.
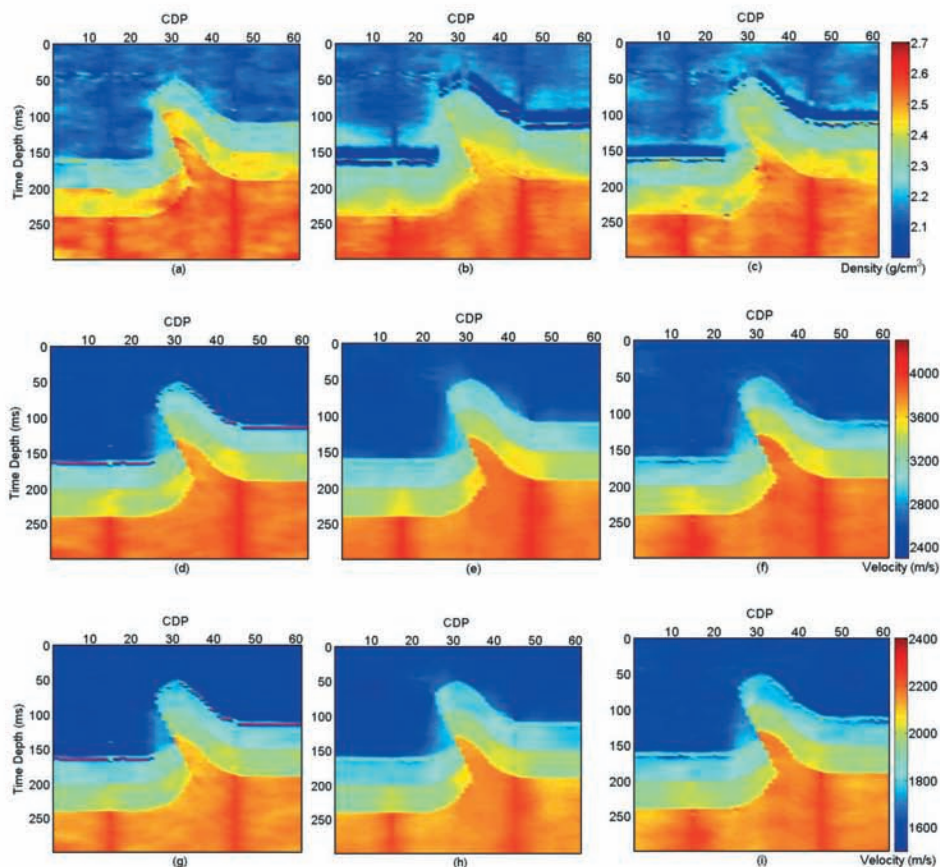
Fig. 5. The inverted results for (a) ρ, (d) V_P, and (g) V_S by using the angle gather of 0°–12°; for (b) ρ, (e) V_P, and (h) V_S by using the angle gather of 21°–33°; and for (c) ρ, (f) V_P, and (i) V_S by using the angle gather of 36°–48°.

   More relative residuals of inverted density are observed (Figs. 6(a)–(c)) when increasing the incidence angle, particularly for these along the fault and near the interfaces. However, for the inverted results of V_P (Figs. 5(d)–(f)) and V_S (Figs. 5(g)–(i)), we find that they have a little discrepancy between each other for a given angle gather, due to the relatively strong correlation between V_P and V_S. Moreover, the inverted V_P and V_S by using the angle gather of 21.0°–33.0° (Figs. 5(e) and 5(h)) and 36.0°–48.0° (Figs. 6(f) and 6(i)) are better, in which the features along the fault is clearly revealed, and this is also demonstrated by comparing the residuals shown in Figs. 6(d)–(i). Therefore, because of density's larger reflectivity contribution at small incidence angle, we can obtain fine density results by using small incidence angle based on the proposed inversion method. In addition, for inverting velocities, moderate or large incidence angle gather is recommended.
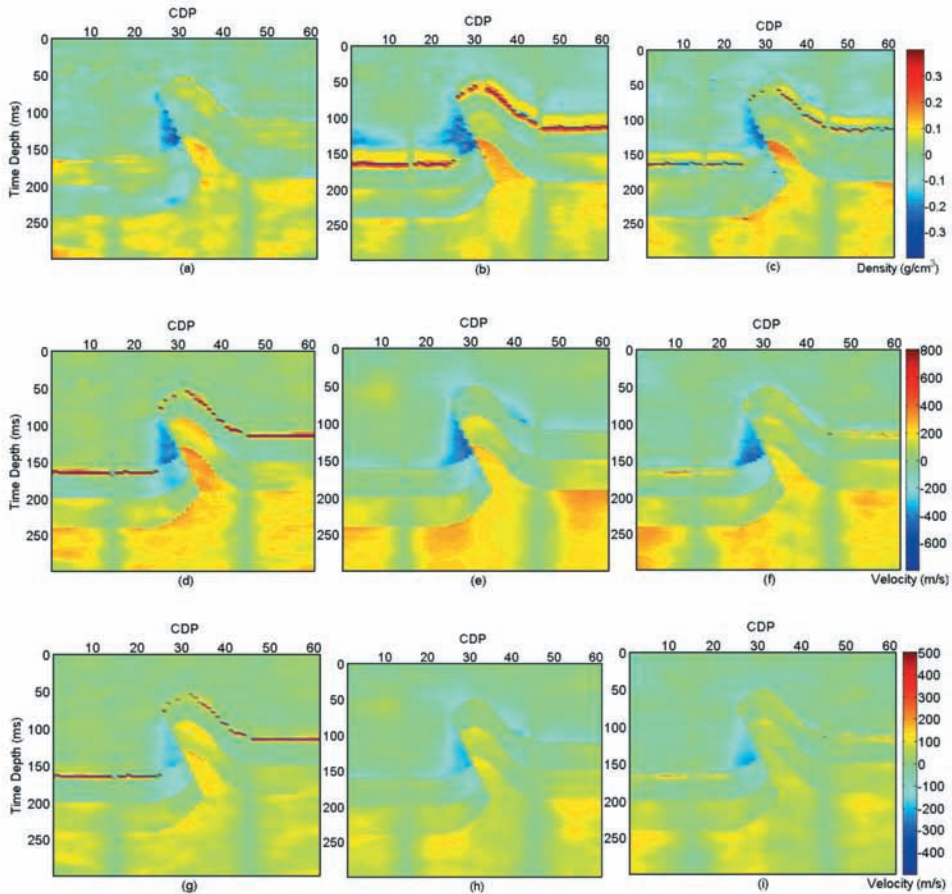
Fig. 6. Relative residuals of (a) ρ, (d) V_P, and (g) V_S by using the angle gather of 0°–12°; for (b) ρ, (e) V_P, and (h) V_S by using the angle gather of 21°–33°; and for (c) ρ, (f) V_P, and (i) V_S by using the angle gather of 36°–48°, with the corresponding true models (in Figs. 4a–c), respectively. Note the relatively small residuals, particularly for those along the fault and near the interface by using the small incidence angle for the density results.
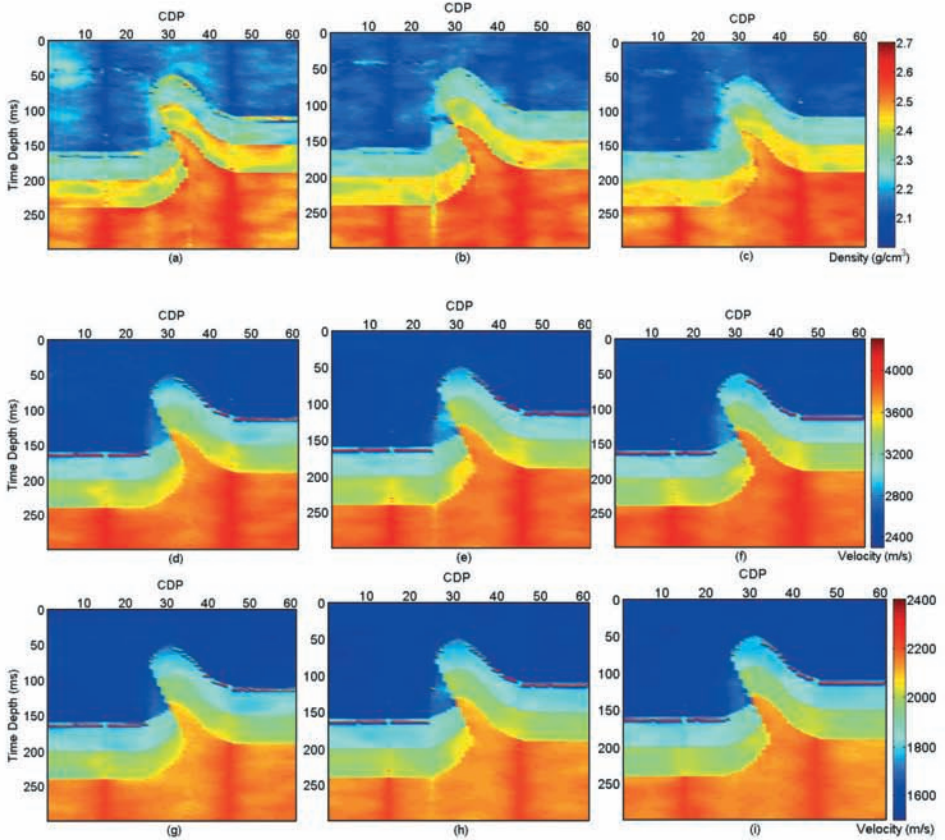
Fig. 7. The inverted results for (a) ρ, (d) V_P, and (g) V_S by multiplying density's (J_{2D}) weighting coefficient of 0.6; for (b) ρ, (e) V_P, and (h) V_S by multiplying density's (J_{2D}) weighting coefficient of 0.8; and for (c) ρ, (f) V_P, and (i) V_S by multiplying density's (J_{2D}) weighting coefficient of 1.2.

Improving the results of density by adjusting the prior term

In the previous inverted results, the results of density are relatively worse than those of V_P or V_S. Furthermore, we attempt to improve the result of density by adjusting the scaling parameter δ_D of the density prior term J_{2D} in eq. (7), i.e., increasing the value of δ_D. But it only produces little effect on the result of density because over-larger δ_D value adversely leads an unstable result. Therefore, we attempt to improve the result of density by directly scaling the prior term J_{2D}, i.e., adjusting the density prior term by multiplying a weighting coefficient λ_D in eq. (7).
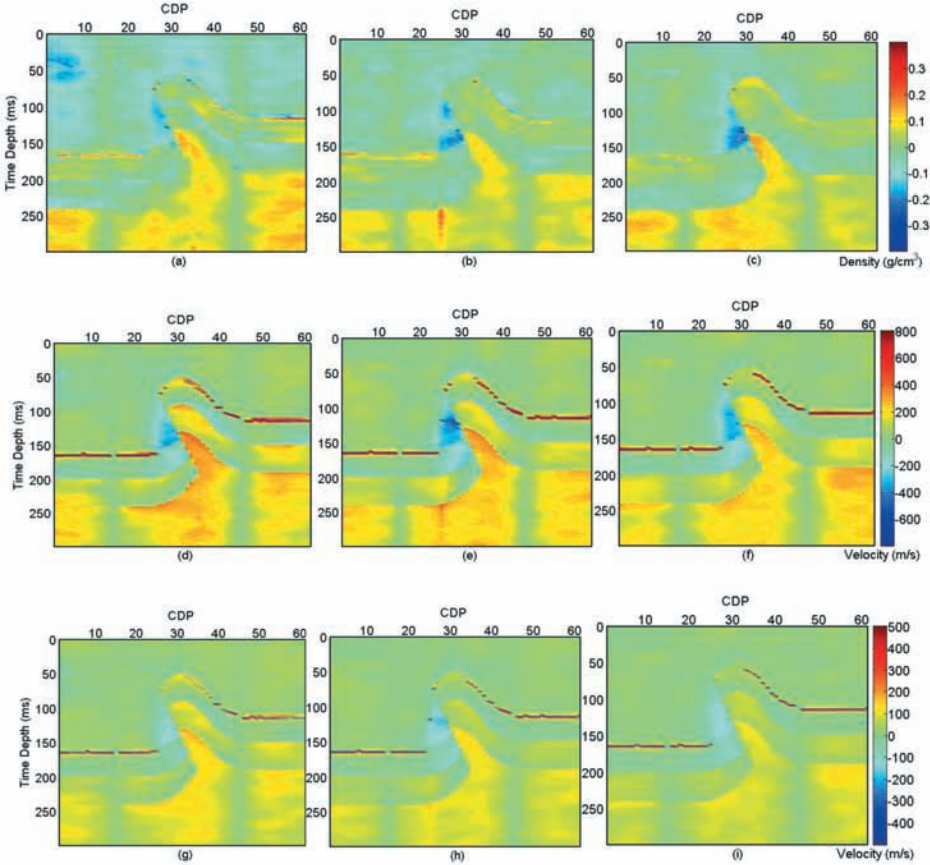
Fig. 8. Relative residuals of (a) ρ, (d) V_P, and (g) V_S by multiplying density's (J_{2D}) weighting coefficient of 0.6; for (b) ρ, (e) V_P, and (h) V_S by multiplying density's (J_{2D}) weighting coefficient of 0.8; and for (c) ρ, (f) V_P, and (i) V_S by multiplying density's (J_{2D}) weighting coefficient of 1.2, with the corresponding true models (in Figs. 4a–c), respectively. Note the decreased residuals along the fault and near the interface with increasing the weighting coefficient for the density results.

Here, we tested the synthetic data by varying the weighting coefficients of the density prior term, which are 0.6, 0.8, and 1.2, respectively. Figs. 7(a)–(i) shows the inverted results of density, V_P, and V_S by using the (three) weighting coefficients of J_{2D}, respectively, and Figs. 8(a)–(i) shows the residuals of the inverted results with the corresponding true models, respectively. For the inverted results of density (Figs. 7(a)–(c)), we find that the inverted density by using the larger weighting coefficient (Fig. 7(c)) is better; this is also demonstrated by comparing the three residuals in Figs. 8(a)–(c), since the inverted results of the density become closer to the true model with increasing the weighting coefficient. However, the inverted results of V_P and V_S show the opposite trend. Those indicated we can improve the density results by scaling the corresponding prior term; however, it is difficult to simultaneously gain fine results of the three

parameters. The improvement of the result of density is usually at a sacrifice of the results of V_P or V_S.
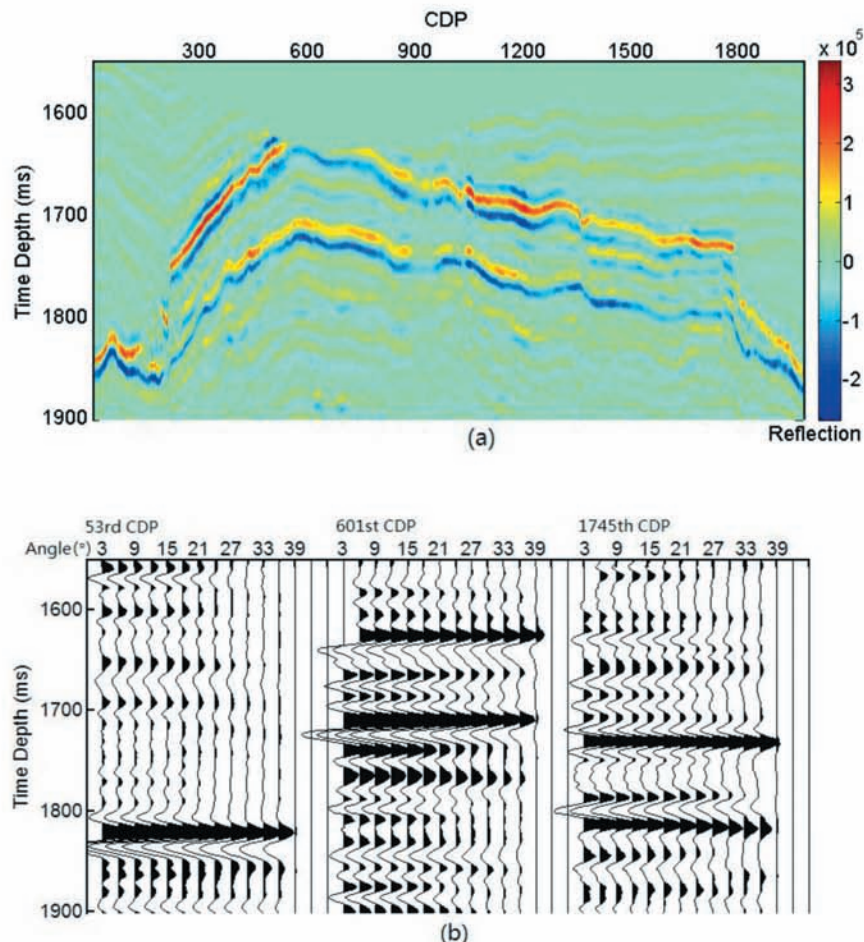

(a)

(b)

Fig. 9. (a) The stacked seismic section of the field data. This section has three wells locating at 53rd, 601st, and 1745th CDP; (b) The original angle gathers at the well location.

FIELD DATA EXAMPLE

We further tested the inverted density result on 2D field data from the South China Sea to gain confidence in our conclusion. The 2D prestack seismic data has 1981 CDPs with an interval of 12.5 m and 165 samples with a sampling rate of 2 ms, and has three logs (Wells 1, 2, and 3) which are located at 53rd, 601st, and 1745th CDPs, respectively. Fig. 9(a) depicts the stacked seismic section of the field data and Fig. 9(b) shows the corresponding angle gathers near the three Wells. The incidence angles for each angle gather are from 3° to 42° with an angle interval of 3°. We

estimated three angle wavelets by the constrained least-squares method, with zero-phase and the dominant frequencies of 30–35 Hz, shown in Fig. 10. In addition, the initial models of V_P and density (see Fig. 11) are built by using the parameter values of several main layers extracted from the well logs, and the initial value of V_S is built as a function of V_P. There is a low correlation value of 0.477 between the synthetic seismogram of the initial models and the original prestack seismic data. The optimization approach and the selected regularization parameter values are the same as those used in the synthetic data test. In addition, we used multiple MRF order neighbourhoods during the annealing process, i.e., using first-order when annealing temperature $T < 0.001$, second-order when $0.001 < T < 0.005$, and third-order when $T > 0.005$.
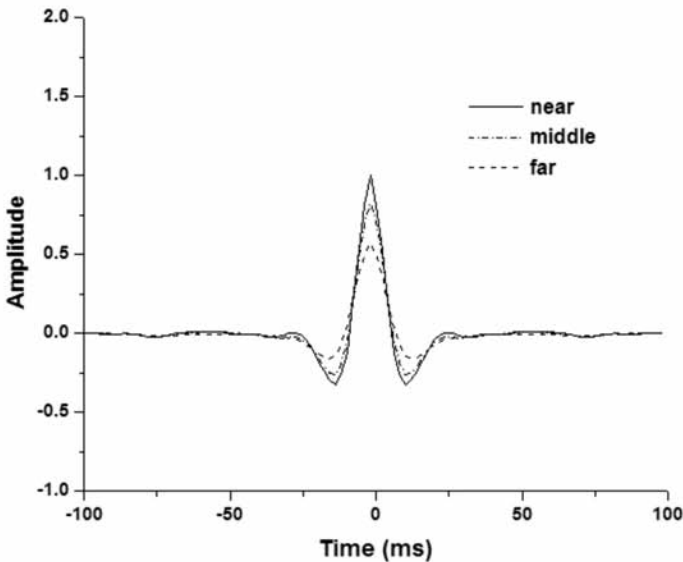

Fig. 10. The estimated source wavelets at Well 3 location by the constrained least-squares method. These are the zero-phase wavelets with the peak frequencies of 30–35 Hz.

Figs. 12–14 show the multiparameter inverted results by using the three angle gathers of 3°–15°, 21°–30°, and 30°–36°, respectively. Comparing the density results shown in Figs. 13(a)–(c), in which we can identify most of the main structures. In particular, the one by using the small angle gather demonstrates better performance in resolving the structural details (marked by the arrow in Fig. 12(a)). Comparing the V_P results show in Figs. 13(a)–(c), it seems that the one by using the moderate angle gather shows better resolution in revealing the top of the target layer (marked by the arrows in Fig. 13(b)). Similarly, the V_S result by using the moderate angle gather demonstrates better resolution (marked by the arrows in Fig. 14(b)). The unsatisfactory inverted velocity results by using large angle gather may result from the NMO stretch and offset-dependent tuning occurred in the far-offset prestack data.
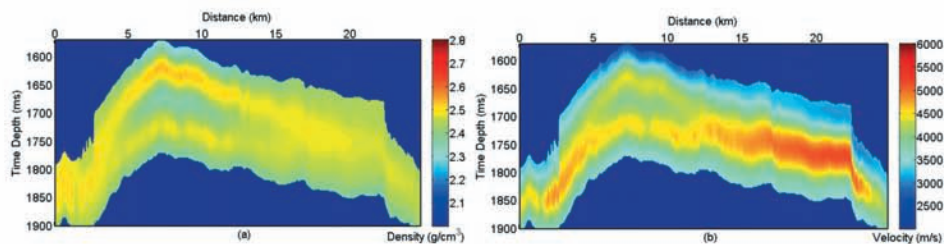
Fig. 11. The initial models of (a) density and (b) V_P, built by smoothing the logging data of several main layers.

Furthermore, Fig. 15 shows the comparison between the inverted results (shown in Figs. 12–14) in 1745th CDP and the logging curves in Well 3. We can observe that the general shape of the inverted results and the logging curves shows good agreement and the structural boundaries are revealed. The agreement for inverted V_P and V_S, by using the angle gather from 21° to 30° (middle chart in Figs. 15(a)–(b)), are better than those of others. In the agreement for inverted density, the one by using the angle gather from 3° to 15° (upper chart in Fig. 15(c)) is better, especially between the section of 1780–1810 ms. This, once again, demonstrated that we can obtain satisfactory density results by using small angle gather; in order to invert the velocity models, using moderate angle gather is a good choice.
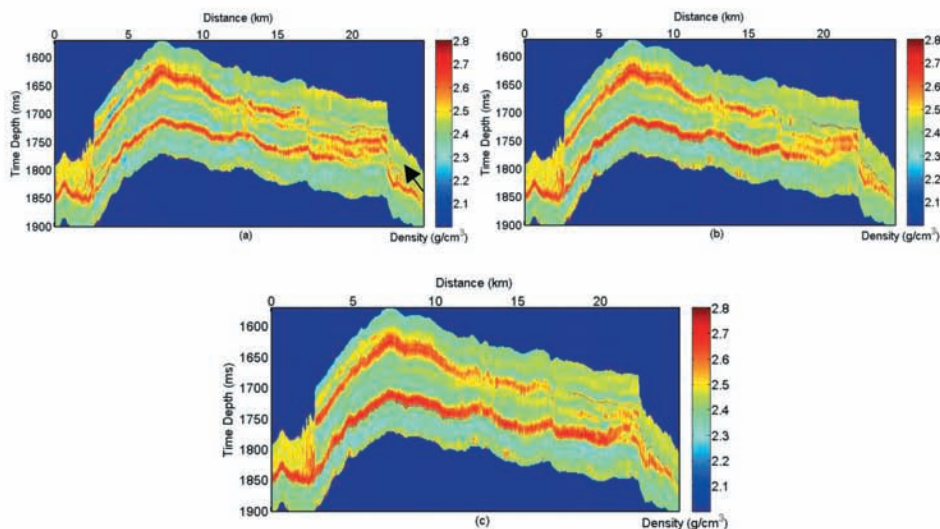

Fig. 12. The inverted density model by using the angle gather (a) from 3° to 15°, (b) from 21° to 30°, and (c) from 30° to 36°, respectively. The arrow indicates the structural detail within the target layer.
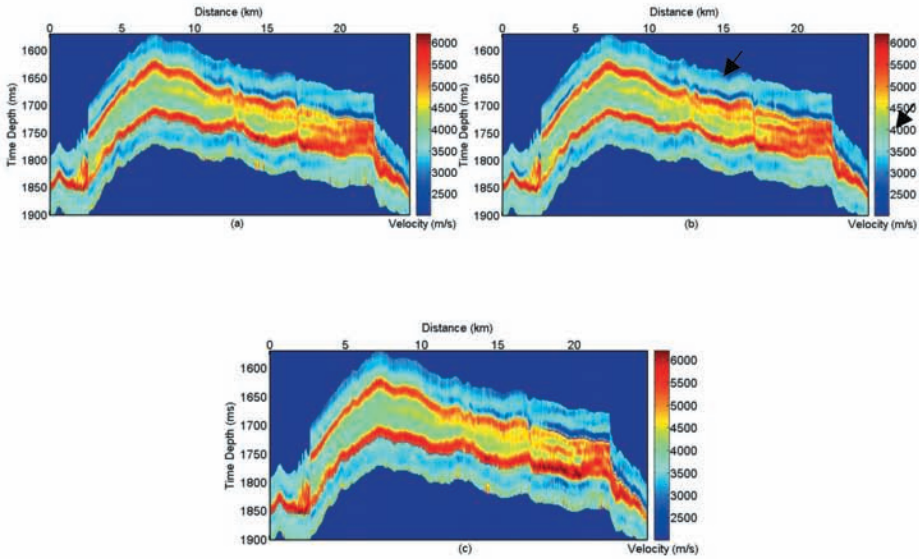
Fig. 13. The inverted V_P model by using the angle gather (a) from 3° to 15°, (b) from 21° to 30°, and (c) from 30° to 36°, respectively. The arrows indicate the top of the target layer.
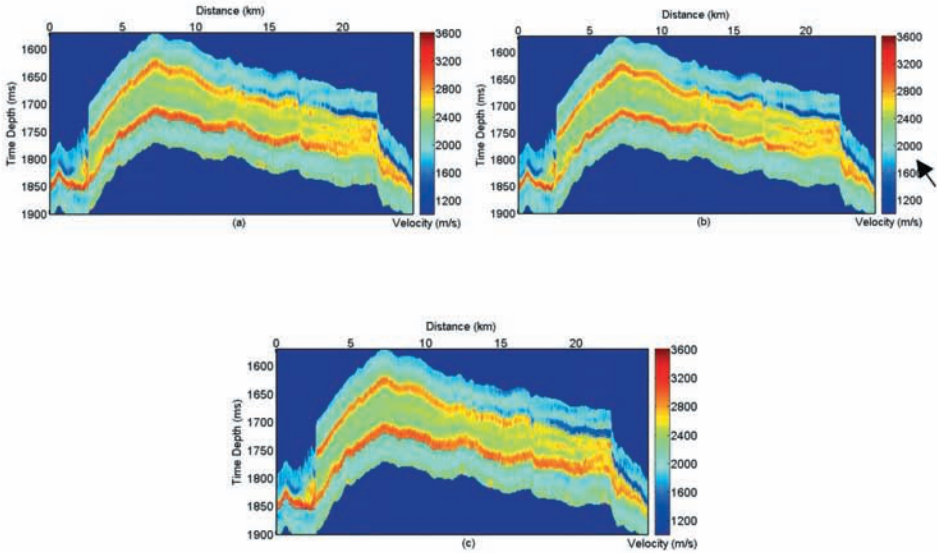

Fig. 14. The inverted V_S model by using the angle gather (a) from 3° to 15°, (b) from 21° to 30°, and (c) from 30° to 36°, respectively. The arrow indicates the structural detail within the target layer.
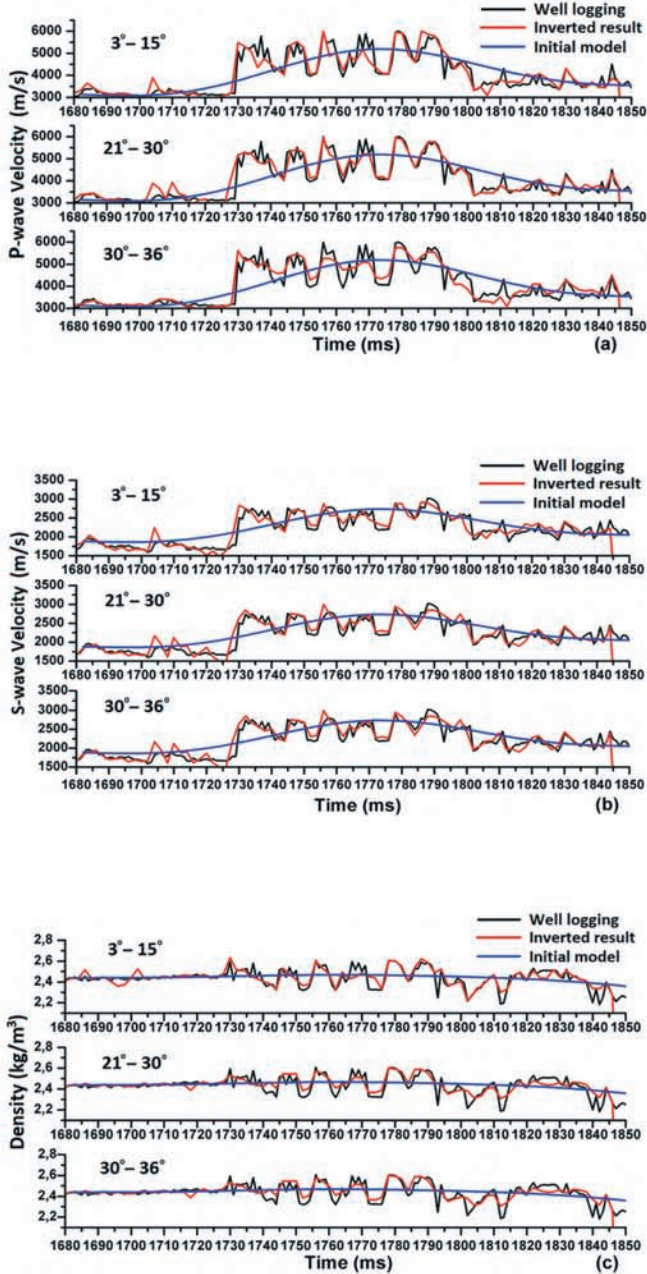
Fig. 15. Comparison between the inverted results (red lines) of (a) V_P, (b) V_S, (c) and density and the corresponding logging curves (black lines) of Well 3. The range of angle gather are from 3° to 15°, from 21° to 30°, and from 30° to 36°, respectively.

CONCLUSION

In this paper, we proposed a nonlinear multiparameter prestack seismic inversion method in order to handle the nonlinearity of prestack inversion and obtain reliable density information. We directly used the exact Zoeppritz equation as the forward operator and constructed the edge-preserving regularized objective function based on the anisotropic Markov random field, together aided with FSA as optimization approach. Special attenuation is focused on the density-sensitivity study based on the angle-dependent contribution on altering the reflectivity magnitude. We demonstrated the proposed inversion method and the conclusion on both 2D synthetic test and field data example.

Numerical analysis indicated that, based on the angle-dependent reflectivity contribution, density is sensitive around small incidence angle and its sensitivity decreases with increasing the incidence angle for all the three AVO models; P- and S-wave velocity are sensitive at moderate or large incidence angle for most of the AVO models.

The test of the synthetic data indicated that better inverted density can be obtained by using small incidence angle; the results of both V_P and V_S, by using the moderate or large incidence angle, are better. Moreover, the inverted result can be improved by adjusting the weighting coefficient of density prior term, i.e., the results of the density become accurate and stable when appropriately increasing the weighting coefficient. However, it is very difficult to simultaneously gain the satisfied results of the three parameters. The attempt to obtain better density results is usually at the cost of the results of S- and P-wave velocity.

In the field data example, we simultaneously obtained the inverted models of V_P, V_S, and density with structural details. Comparing the inverted results with the corresponding logging curves, we see that they show good agreement for most parts. In particular, the density result by using the small angle gather shows better resolution in revealing structural detail.

ACKNOWLEDGMENTS

REFERENCES

Aki, K. and Richards, P.G., 1980. Quantitative Seismology: Theory and Methods. W.H. Freeman and Co., San Francisco.

Aleardi, M. and Mazzotti, A., 2017. 1D elastic full-waveform inversion and uncertainty estimation by means of a hybrid genetic algorithm–Gibbs sampler approach. Geophys. Prosp., 65: 64-85.

Bortfeld, R., 1961. Approximation to the reflection and transmission coefficients of plane longitudinal and transverse wave. Geophys. Prosp., 9: 485-502.

Chapman, M., Liu, E. and Liu, X.Y., 2006. The influence of fluid sensitive dispersion and attenuation on AVO analysis. Geophys. J. Internat., 167: 89-105.

Charbonnier, P., Blanc-Féraud, L. and Aubert, G., 1997. Deterministic edge-preserving regularization in computed imaging. IEEE Transactions on Image Processing, 6: 298–311.

Chen, J., Zhang, Z. and Liu, E., 2006. Anisotropic inversion of traveltimes and polarization of wide-angle seismic data using simulated annealing. J. Seismic Explor., 15: 101-118.

Downton, J. E., 2005. Seismic parameter estimation from AVO inversion. Ph.D. Thesis, University of Calgary.

Downton, J.E. and Ursenbach, C., 2006. Linearized amplitude variation with offset (AVO) inversion with supercritical angles. Geophysics, 71: E49–E55.

Fatti, J.L., Smith, G.C. and Vail, P.J., 1994. Detection of gas in sandstone reservoirs using AVO analysis: A 3-D seismic case history using the Geostack technique. Geophysics, 59: 1362–1376.

Geman, D. and Reynolds, G., 1992. Constrained restoration and the recovery of discontinuities. IEEE Transactions on Pattern Analysis and Machine Intelligence, 14: 367–383.

Geman, D. and Yang, C., 1995. Nonlinear image recovery with half-quadratic regularization. IEEE Transactions on Image Processing, 4: 932–946.

Grossman, J.P., 2003. AVO and AVA inversion challenges: a conceptual overview. CREWES Research Report, 15.

Guo, Q., Zhang, H., Saeed, W. and Shang, Z., 2016. Features of Markov random field about simultaneous inversion of pre-stack seismic data in transversely isotropic media. Extended Abstr., 78th EAGE Conf., Vienna: Th P6 04.

Hilterman, F.J., 2001. Seismic Amplitude Interpretation. Distinguished Instructor Short Course. SEG/EAGE.

Huang, H., Zhang, R., Shen, G., Guo, F. and Wang, J., 2011. Study of prestack elastic parameter consistency inversion methods. Appl. Geophys., 8: 311–318.

Ingber, L., 1989. Very fast simulated re-annealing. Mathemat. Comput. Model., 12: 967-993.

Ji, Y., Singh, S.C. and Hornby, B.E., 2000. Sensitivity study using a genetic algorithm: inversion of amplitude variations with slowness. Geophys. Prosp., 48: 1053-1073.

Kabir, N., Crider, R., Ramkhelawan, R. and Baynes, C., 2006. Can hydrocarbon saturation be estimated using density contrast parameter. CSEG Recorder, 31: 31-37.

Liang, L., Zhang, H., Dan, Z., Xu, Zi, Liu, X. and Cao, C., 2017. Prestack density inversion using the Fatti equation constrained by the P- and S-wave impedance and density. Appl. Geophys., 14: 133-141.

Lines, L.R., 1998. Density contrast is difficult to determine from AVO. CREWES Research Report, 10.

Ma, X.Q., 2002. Simultaneous inversion of prestack seismic data for rock properties using simulated annealing. Geophysics, 67: 1877-1885.

Misra, S. and Sacchi, M.D., 2008. Global optimization with modelspace preconditioning: Application to AVO inversion. Geophysics, 73: R71–R82.

Ostrander, W.J., 1984. Plane-wave reflection coefficients for gas sands at nonnormal angles of incidence. Geophysics, 49: 1637–1648.

Paasche, H. and Tronicke, J., 2014. Nonlinear joint inversion of tomographic data using swarm intelligence. Geophysics, 79: R133-R149.

Sacchi, M.D., Wang, J. and Kuehl, H., 2006. Regularized migration/inversion: new generation of imaging algorithms. CSEG Recorder, 31: 54-59.

Sen, M.K. and Stoffa, P.L., 1996. Bayesian inference, Gibbs' sampler and uncertainty estimation in geophysical inversion. Geophys. Prosp., 44: 313–350.

Sen, M.K. and Stoffa, P.L., 2013. Global Optimization Methods in Geophysical Inversion, Second Ed. Cambridge University Press, Cambridge, UK.

Shuey, R.T., 1985. A simplification of the Zoeppritz equations. Geophysics, 50: 609–614.

Tarantola, A. and Valette, B., 1982. Generalized nonlinear inverse problems solved using the least squares criterion. Rev.Geophys. Space Phys., 20: 219-232.

Tarantola, A., 2005. Inverse Problem Theory and Model Parameter Estimation. SIAM.

Theune, U., Jensas, I. and Eidsvik, J., 2010. Analysis of prior models for a blocky inversion of seismic AVA data. Geophysics, 75: C25–C35.

Ursenbach, C., 2002. Optimal Zoeppritz approximations. Expanded Abstr., 72nd Ann. Internat. SEG Mtg., Salt Lake City:1897-1900.

Varela, O.J., Torres-Verdin, C. and Sen, M.K., 2006. Enforcing smoothness and assessing uncertainty in non-linear one-dimensional prestack seismic inversion. Geophys. Prosp., 54: 239-259.

Yan, Z. and Gu, H., 2013. Non-linear prestack seismic inversion with global optimization using an edge-preserving smoothing filter. Geophys. Prosp., 61: 747-760.

Youzwishen, C.F. and Sacchi, M.D., 2006. Edge preserving imaging, J. Seismic Explor.. 15: 45-58.

Zhang, H., Shang, Z. and Yang, C., 2007. A non-linear regularized constrained impedance inversion. Geophys. Prosp., 55: 819-833.

Zhang, H., Shang, Z. and Yang, C., 2009. Adaptive reconstruction method of impedance model with absolute and relative constraints. J. Appl. Geophys., 67: 114-124.

Zhi, L., Chen, S. and Li, X.Y., 2016. Amplitude variation with angle inversion using the exact Zoeppritz equations - Theory and methodology. Geophysics, 81: N1–N15.

Zong, Z., Yin, X. and Wu, G., 2012. AVO inversion and poroelasticity with P- and S-wave moduli. Geophysics, 77: N17–N24.

Zong, Z., Yin, X. and Wu, G., 2013. Elastic impedance parameterization and inversion with Young's modulus and Poisson's ratio. Geophysics, 78: N35–N42.